# Ab Initio Spatial Phase Retrieval via Fluorescence Intensity Triple Correlations

**Nolan Peard,[1,2] Kartik Ayyer,[2,3,4] and Henry N. Chapman[2,4,5,6,*]**

[1]*Department of Applied Physics, Stanford University, Stanford, CA, USA*
[2]*Center for Free-Electron Laser Science, Deutsches Elektronen Synchrotron DESY, Hamburg, Germany*
[3]*Max Planck Institute for the Structure and Dynamics of Matter, Hamburg, Germany*
[4]*The Hamburg Center for Ultrafast Imaging, Universität Hamburg, Hamburg, Germany*
[5]*Department of Physics, Universität Hamburg, Hamburg, Germany*
[6]*Molecular and Condensed Matter Physics, Department of Physics and Astronomy, Uppsala University, Uppsala, Sweden*
[*]*henry.chapman@cfel.de*

**Abstract:** A complete method for ab initio phase retrieval via spatial intensity triple correlations is described. Simulations demonstrate accurate phase retrieval for clusters of classical incoherent emitters.



## 1. Introduction

Coherent diffractive imaging uses the far-field interference of elastically-scattered light to infer the geometry of a scattering potential via Fourier analysis. Since square-law detectors can only make intensity measurements, information about the relative phases $\phi(\vec{m})$ of the scattered waves at pixels $\vec{m}$ is usually lost and any Fourier inversion to real space remains necessarily incomplete [1]. A large section of the x-ray crystallography literature deals with experimental and data processing techniques to retrieve this critical phase information with anomalous scattering, molecular replacement, and direct methods among other techniques.

Intensity triple correlations have been known to reveal the phase of scattered waves via the *closure phase* since the 1960s [2, 3] and have found limited application in radio astronomy [4–8]. Recent work has examined the possibility of using photon pair correlations to retrieve coherent diffraction patterns from x-ray fluorescence [9–13] and to perform pulse metrology of x-ray light sources [14, 15]. If phase retrieval for crystallography via x-ray photon triple correlations is to be attempted, we must fill in some gaps in the available algorithms.

As will be shown in the next section, the triple correlations allow relatively straightforward computation of the absolute value of the *closure phase*, $|\Phi(\vec{m},\vec{n})| = |\phi(\vec{m}+\vec{n}) - \phi(\vec{m}) - \phi(\vec{n})|$. Clearly, the signed value of $\Phi$ is required to recover the phase information $\phi(\vec{m})$. At the start of phase extraction, an arbitrary value is chosen for the first pixel. For subsequent pixels, however, the sign of the *closure phase* must be determined using redundant information contained in $|\Phi(\vec{m},\vec{n})|$. Multiple publications have described this concept but, to the best of our knowledge, no one has yet provided a useful explanation of how to calculate $\mathrm{sgn}(\Phi(\vec{m},\vec{n}))$ [16–29]. Ab-initio phase retrieval from the third-order intensity correlations has thus remained incomplete for decades.

In this paper, we describe how the sign problem is solved and show a numerical implementation of our method with simulated data from classical light sources.

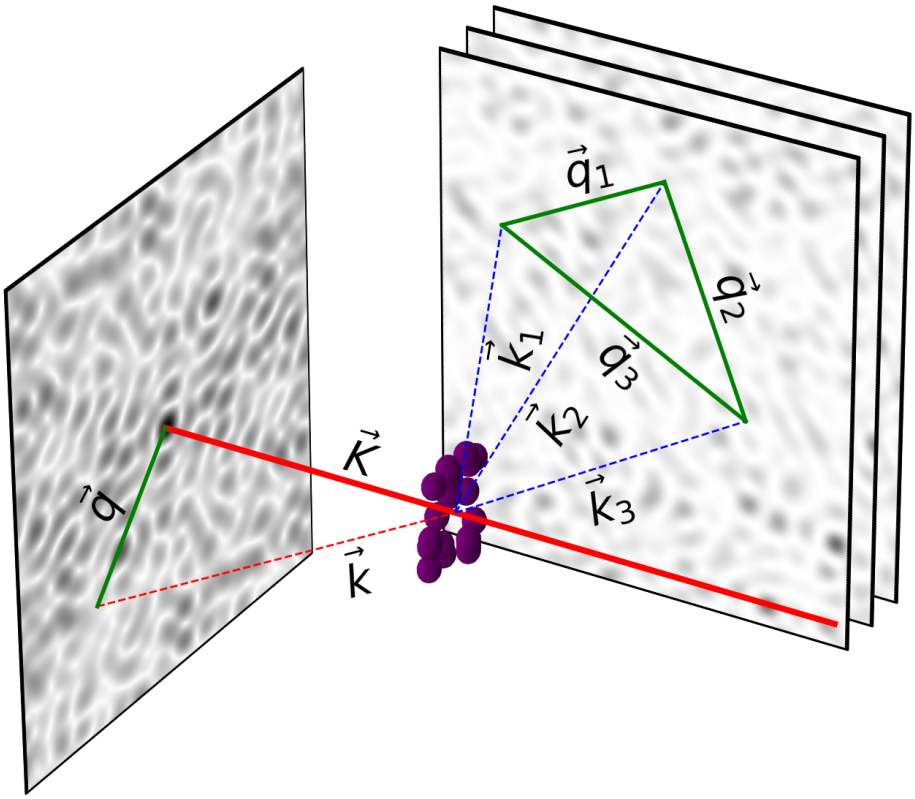


Fig. 1. Schematic sketch of coherent diffraction in the forward detection plane, intersecting with the incident beam $\vec{K}$. Fluorescence speckle is emitted by the atoms isotropically and the position of the second detector is not dependent on the incident beam. Coherent diffraction data is collected as a function of the scattering vector $\vec{q} = \vec{K} - \vec{k}$. Correlations between triples of fluorescence photons at pixels separated by $\vec{q}_1$, $\vec{q}_2$, and $\vec{q}_3$ reveal the spatial phase information lost in the coherent diffraction experiment.

## 2. Theory

In what follows, we define the photon scattering vectors in reciprocal space

$$\vec{q}_1 = \vec{k}_1 - \vec{k}_2 \tag{1}$$

$$\vec{q}_2 = \vec{k}_2 - \vec{k}_3 \tag{2}$$

$$\vec{q}_3 = \vec{k}_3 - \vec{k}_1 = -\vec{q}_1 - \vec{q}_2 \tag{3}$$

as depicted in Figure 1. We use the word *atom* to refer to any member of a collection of point fluorescent (or thermal, in the case of stars) light sources. We assume these atoms to undergo spontaneous emission independently, i.e. that each atom emits a field with a phase or time delay that is uncorrelated to the fields emitted by the other atoms. The total light field in this scenario

is often referred to as pseudo-thermal or chaotic and has intensity

$$I(\vec{k}) = \left| \sum_{i}^{\nu} s_i e^{i(\vec{k}\cdot\vec{r}_i + \phi_i)} \right|^2 = \sum_{ij} s_i s_j^* e^{i(\phi_i - \phi_j)} e^{i\vec{k}\cdot(\vec{r}_i - \vec{r}_j)} \tag{4}$$

where the $\phi_i$ are random, uncorrelated phases which vary on timescales greater than the relevant system coherence time, $\tau_c$. When rapid exposures are measured with a photodetector, we can consider these phases to reset shot-to-shot. The sum is taken over the total number of atoms, $\nu$. $\vec{r}_i$ and $s_i$ are the position and amplitude of electric field emission by the $i$th atom. From the right-hand side of this equation, we observe that the structure ($\vec{r}_i$ for all $i$) would be difficult to acquire by averaging intensities over many shots - the random phase resets would drive the interference fringe visibility to zero. However, it remains possible to obtain structural information via intensity correlations [9].

The ensemble average of third-order intensity correlations of this light field over all shots

$$\left\{ g^{(3)}(\vec{k}_1, \vec{k}_2, \vec{k}_3) \right\} = \left\{ \frac{\langle I(\vec{k}_1) I(\vec{k}_2) I(\vec{k}_3) \rangle}{\langle I(\vec{k}_1) \rangle \langle I(\vec{k}_2) \rangle \langle I(\vec{k}_3) \rangle} \right\} \tag{5}$$

can be expressed as

$$\left\{ g^{(3)}(\vec{q}_1, \vec{q}_2) \right\} \approx \left(1 - \frac{3}{\nu} + \frac{4}{\nu^2}\right) + \left(1 - \frac{2}{\nu}\right) \left( |g^{(1)}(\vec{q}_1)|^2 + |g^{(1)}(\vec{q}_2)|^2 + |g^{(1)}(-\vec{q}_1 - \vec{q}_2)|^2 \right) \tag{6a}$$

$$+ 2\mathrm{Re}\left( g^{(1)}(\vec{q}_1) \quad g^{(1)}(\vec{q}_2) \quad g^{(1)}(-\vec{q}_1 - \vec{q}_2) \right) \tag{6b}$$

and is called the *bispectrum*. Similarly, the mean second-order intensity correlation function

$$\left\{ g^{(2)}(\vec{k}_1, \vec{k}_2) \right\} = \left\{ \frac{\langle I(\vec{k}_1) I(\vec{k}_2) \rangle}{\langle I(\vec{k}_1) \rangle \langle I(\vec{k}_2) \rangle} \right\} \tag{7}$$

may be written as

$$\left\{ g^{(2)}(\vec{q}_1) \right\} \approx 1 - \frac{1}{\nu} + \left| g^{(1)}(\vec{q}_1) \right|^2 \tag{8}$$

This equation is often referred to as the Siegert Relation in quantum optics. For a full derivation of Equations 6 and 8 please review the Appendix.

We have here an expression for $g^{(3)}$ in terms of constants, the square modulus of $g^{(1)}$, and the real part of a product of complex-valued $g^{(1)}$. Since $\left|g^{(1)}\right|$ may be acquired from $g^{(2)}$, it is possible to extract the last term 6b alone. This term is referred to as the *closure* in the astronomy literature. We can rewrite the *closure* as

$$2\mathrm{Re}\left( g^{(1)}(\vec{q}_1) \quad g^{(1)}(\vec{q}_2) \quad g^{(1)}(-\vec{q}_1 - \vec{q}_2) \right) =$$
$$2 \left| g^{(1)}(\vec{q}_1) \right| \left| g^{(1)}(\vec{q}_2) \right| \left| g^{(1)}(-\vec{q}_1 - \vec{q}_2) \right| \cos\left( \phi(\vec{q}_1) + \phi(\vec{q}_2) + \phi(-\vec{q}_1 - \vec{q}_2) \right) \tag{9}$$

where we have rendered $g^{(1)}$ in polar coordinates in the complex plane. As the radial component ($\left|g^{(1)}\right|$) is easily obtained from $g^{(2)}$, the phase information ($\phi(\vec{q})$) can be isolated as follows.

Suppose we set $\vec{q}_1 = \vec{m}$ and $\vec{q}_2 = \vec{n}$ where $\vec{m}$, $\vec{n}$ map to discrete pixels on a detector. The symmetry of $\left|g^{(1)}(\vec{q})\right|$ and anti-symmetry of $\phi(\vec{q})$ (see Appendix 6.6 to review Friedel's Law)

allow us to rearrange the *closure* into

$$\cos\Big(\phi(\vec{m}+\vec{n})-\phi(\vec{m})-\phi(\vec{n})\Big)\approx \frac{g^{(3)}(\vec{m},\vec{n})-(1-\frac{3}{\nu}+\frac{4}{\nu^2})-(1-\frac{2}{\nu})(|g^{(1)}(\vec{m})|^2+|g^{(1)}(\vec{n})|^2+|g^{(1)}(\vec{m}+\vec{n})|^2)}{2\left|g^{(1)}(\vec{m})\right|\left|g^{(1)}(\vec{n})\right|\left|g^{(1)}(\vec{m}+\vec{n})\right|} \tag{10}$$

The inverse cosine of this expression is known as the *closure phase*, which we represent via the symbol

$$\Phi(\vec{m},\vec{n}) = \pm\left[\phi(\vec{m}+\vec{n})-\phi(\vec{m})-\phi(\vec{n})\right] \tag{11}$$

Just as in the Siegert Relation, the third-order correlation function encodes the phase $\phi(\vec{q})$ at pixels in k-space beyond the physical spatial extent of the detector ($|\vec{q}_{\max}| = 2\left|\vec{k}_{\max}\right|$). Together, the double and triple correlations allow retrieval of the coherent diffraction pattern *and* its phase across an area of k-space four times larger than the area of detector coverage.

## 3. Phase Retrieval

The *closure phase* is a difference equation which can be used like a discrete derivative to estimate the slope of $\phi(\vec{q})$ between pixels separated by $\vec{n}$. The anti-symmetry of the phase pins $\phi(\vec{q}=\vec{0})=0$. We make an assumption of the value of the phase at a nearest-neighbor pixel of $\phi(\vec{q}=\vec{0})=0$. The difference equation and calculated $\Phi(\vec{m},\vec{n})$ from experimental data reveals the value of the phase at the next-nearest-neighbor pixels and so forth until the phase on the entire pixel array has been calculated.

Once the second pixel of $\phi$ (next-nearest neighbor) in any direction is calculated, the interval of the difference equation ($\vec{n}$) may be increased to find the slope between every other (instead of every) pixel in the same direction. Essentially, the phase values calculated for pixels near the origin constrain the possible phase values of pixels far from the origin.

### *3.1. Determining sgn*($\Phi$)

Due to the sign ambiguity of the inverse cosine, every datum from $\Phi(\vec{m},\vec{n})$ points to two possible values of the phase $\phi(\vec{m}+\vec{n})$

$$\phi(\vec{m}+\vec{n}) = +\Phi(\vec{m},\vec{n})+\phi(\vec{m})+\phi(\vec{n}) \equiv \theta_+ \tag{12}$$

or

$$\phi(\vec{m}+\vec{n}) = -\Phi(\vec{m},\vec{n})+\phi(\vec{m})+\phi(\vec{n}) \equiv \theta_- \tag{13}$$

for any $\vec{m}$ and $\vec{n}$. Assuming a global sign often leads to an incorrect slope for $\phi$, as shown in Figure 2. The fact that multiple values of $\Phi(\vec{m},\vec{n})$ relate to the value of the phase at a single pixel allows us to determine the proper sign of $\Phi(\vec{m},\vec{n})$ for each $\vec{m}$ and $\vec{n}$.

Suppose for a given pixel at $\vec{u}$ there exist $N$ sets $(\vec{m},\vec{n})$ in $\Phi(\vec{m},\vec{n})$ for which $\vec{m}+\vec{n}=\vec{u}$. Each set offers a pair of possible values for $\phi(\vec{u})$, giving $2N$ possible values for $\phi(\vec{u})$ altogether. We know that each and every one of the $N$ pairs contains the correct value, so comparing the $N$ pairs should reveal it. Ideally, the correct value is included $N$ times between the $N$ pairs and is found simply by taking the intersection of all pairs. Next, we show a simple 1D example to illustrate the principle.

#### 3.1.1. 1D Example

Suppose we have a $\phi(m) = (0,1,-3,-1,4,2,7)$ for $m=[0,6]$. We can calculate a matching $\Phi(m,n)$ to which we add a sign ambiguity. (We will render our $\Phi(m,n)$ matrix with $mn$-axes

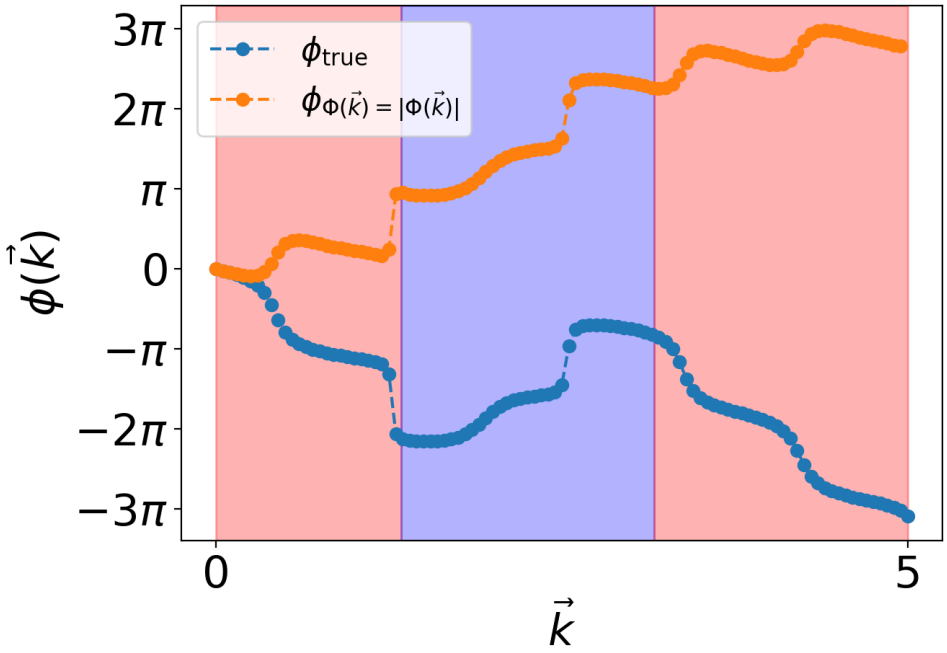


Fig. 2. Phase retrieved for a 1D detector assuming $\Phi(\vec{m},\vec{n}) = |\Phi(\vec{m},\vec{n})|$. The correct contour is recovered with the wrong slope in the sections highlighted in red. The green highlight section has both the correct shape and slope, but is offset due to incorporation of incorrect $\phi$ early in the solution.

such that the origin is in the bottom left corner, i.e. so that $\Phi(1,1) = 5$).

$$|\Phi| = \begin{pmatrix} 0 & & & & & & \\ 0 & 4 & & & & & \\ 0 & 3 & 6 & & & & \\ 0 & 4 & 6 & 9 & & & \\ 0 & 1 & 10 & 6 & 6 & & \\ 0 & 5 & 1 & 4 & 3 & 4 & \\ 0 & 0 & 0 & 0 & 0 & 0 & 0 \end{pmatrix} \tag{14}$$

The upper right corner has no $m + n \leq 6$ and the difference equation 11 is undefined.

Let us assume we have correctly estimated $\phi(1) = 1$. Then, we can try to determine $\phi(2)$ via

$$\Phi(1,1) = |\phi(2) - 2\phi(1)| = 5 \tag{15}$$

which gives the following options

$$\phi(2) = 5 + 2\phi(1) = 7 \tag{16}$$

or

$$\phi(2) = -5 + 2\phi(1) = -3 \tag{17}$$

Since this is a 1D example there is no other point $(m, n)$ such that we can deduce the correct value using $\Phi(m, n)$. The same is true for the calculation of $\phi(3)$ since we only have the information $\Phi(1, 2) = 1$ available to us. For the purposes of this example, we will follow the branch we know to be correct with $\phi(2) = -3$ and $\phi(3) = -1$.

Now the core principle of our algorithm will be demonstrated. We want to find $\phi(4)$ using $\phi(1)$, $\phi(2)$, $\phi(3)$, $\Phi(2, 2)$, and $\Phi(1, 3)$. We then have an additional constraint on $\phi(4)$ via $\Phi(1, 3)$,

$$\phi(4) = \pm\Phi(2, 2) + 2\phi(2) = \pm 10 + -6 \tag{18}$$

$$\phi(4) = \pm\Phi(1, 3) + \phi(1) + \phi(3) = \pm 4 + 0 \tag{19}$$

which gives us four possible values of $\phi(3)$ in two pairs labeled by the points on the $\Phi$ matrix they are associated with ($\Phi(2, 2) \rightarrow \{4, -16\}$ and $\Phi(1, 3) \rightarrow \{4, -4\}$). If we assume that our calculation of $\phi$ up to $\phi(3)$ is accurate, then we should expect that the correct value of $\phi(n = 4)$ is contained in *both* pairs. Examining the intersection of $(4, -4)$ and $(4, -16)$, we may infer that $\phi(4) = 4$.

Similarly, we may determine the correct value and sign of $\phi(5)$ via two constraints from $|\Phi|$.

$$\phi(5) = \pm\Phi(2, 3) + \phi(2) + \phi(3) = \pm 6 + -4 \rightarrow \{2, -10\} \tag{20}$$

$$\phi(5) = \pm\Phi(1, 4) + \phi(1) + \phi(4) = \pm 3 + 5 \rightarrow \{8, 2\} \tag{21}$$

Again, the intersection of the pairs of possible solutions gives the correct answer $\phi(5) = 2$.

The last entry requires finding the intersection among three pairs since there are three non-redundant pieces of data in $|\Phi|$ we may use.

$$\phi(6) = \pm\Phi(3, 3) + \phi(3) + \phi(3) = \pm 9 - 2 \rightarrow \{7, -11\} \tag{22}$$

$$\phi(6) = \pm\Phi(2, 4) + \phi(2) + \phi(4) = \pm 6 + 1 \rightarrow \{7, -5\} \tag{23}$$

$$\phi(6) = \pm\Phi(1, 5) + \phi(1) + \phi(2) = \pm 4 + 3 \rightarrow \{7, -1\} \tag{24}$$

The intersection of the three pairs leads us to conclude that $\phi(6) = 7$.

### *3.2. Numerical Algorithm*

In practice, the intersection is never exact and a numerical estimation subject to input noise is required. We devised an algorithm to accurately find the intersection of all pairs of possible solutions. Dividing the pairs of solutions for each $\vec{u}$ into two sets, let $(\theta_+, \theta_-)$ be the solution pairs for $\pm\Phi(\vec{m}, \vec{n})$. $\theta_+$ and $\theta_-$ are correlated such that they define horizontal and vertical lines when plotted as ordered pairs in the plane, $(\theta_+, \theta_-)$ and $(\theta_-, \theta_+)$. The intersection of these lines is the intersection of the pairs of possible solutions. It is simpler to consider ordered pairs $(\cos(\theta_+), \sin(\theta_-))$ and $(\cos(\theta_-), \sin(\theta_+))$ to constrain the search to $\phi \in [-\pi, \pi]$ and remove $2\pi$ offsets of the value of $\theta_\pm$ (see Figure 3A). Finding the intersection given some noise in the data $\theta_\pm$ amounts to the minimization of the error function

$$E(\phi) = \sum_i \min\left[(\cos(\theta_\pm)_i - \cos(\phi))^2, (\sin(\theta_\mp)_i - \sin(\phi))^2\right] \tag{25}$$

where the sum is over the $N$ pairs of possible solutions for our chosen $\vec{u}$. The optimal value is the desired value of $\phi$ at $\vec{u}$, $\phi(\vec{u}) = \phi_{\text{opt}}$.

The landscape of the error function $E(\phi)$ presents challenges for optimization because it contains multiple local minima separated by large barriers. An example is shown in Figure 3B. Since the value of the phase needs to be optimized for each pixel on the detector, a rapid and accurate method of determining the absolute minimum is desired. This is most straightforwardly

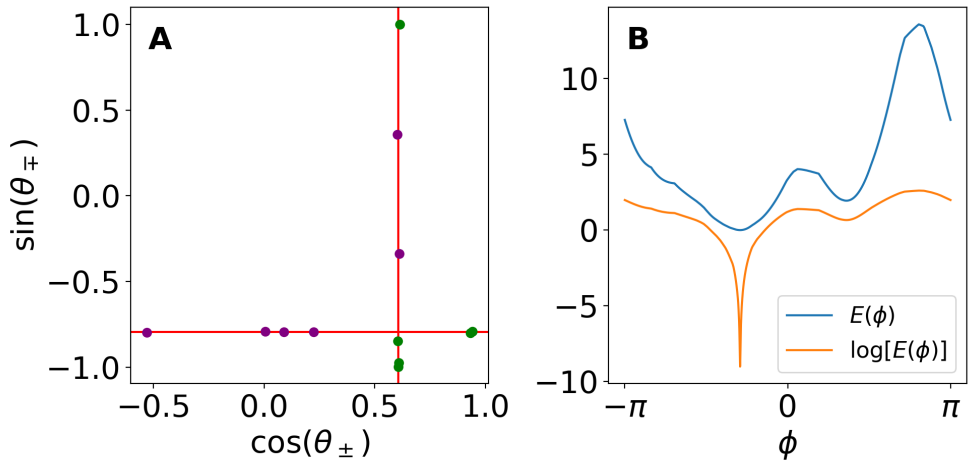


Fig. 3. Successful minimization of the error function $\log E(\phi)$ in (B) finds the correct intersection of the set of $\theta_\pm$ in figure (A). Points in green are the ordered pairs $(\cos\theta_+, \sin\theta_-)$ while points in purple are the ordered pairs $(\cos\theta_-, \sin\theta_+)$, as described in the main text.

accomplished by supplying an optimization algorithm with the minimum value of $\log E(\phi)$ on a grid in $[-\pi, \pi]$; the logarithm increases the contrast of the absolute minima significantly, allowing accurate calculation of an initial guess for the optimizer. The optimizer polishes the brute-force search to a precise final value.

Since the value of $\phi(\vec{m}+\vec{n})$ depends on previous values of $\phi(\vec{m})$ and $\phi(\vec{n})$, it is especially important that values calculated early in the retrieval are accurate. Depending on the quality of the data in $\Phi(\vec{m}, \vec{n})$, the error function may present multiple deep local minima which cause the algorithm to, initially, choose an incorrect value of $\phi$. In this case, $\log[E(\phi)]$ for subsequent pixels in the retrieval sharply increases, indicating that at least one previous pixel has $\phi$ assigned incorrectly. Plotting the total fit error for all pixels indicates the location of problematic pixels which require resolving by toggling candidate phase values until the total error of all pixels is minimized. The consequences of toggling alternate values of $\phi$ near the origin to minimize the error across all pixels are illustrated nicely in Figure 4 by comparing the boxed and unboxed figures.

## 4. Results

Using Equation 10 and the algorithm described in Section 3, we can calculate the Fourier phase from triple correlation data and compare the result to the true value. Figure 4 shows the results of phase retrieval in a simulation with a 2D pixel detector. Note that in regions where the error Figure 4B is small, the solved phase matches the true phase quite well. In this example, sufficient phase information is retrieved to fully resolve the seven simulated atoms (blue circles in Figure 4D) with only $10^4$ shots. The Fourier inversion was performed using the phase retrieved via our algorithm from the third-order correlation function and $\left|g^{(1)}\right|$ calculated via the second-order correlation function. No use of coherent diffraction data was required.

Acquiring additional shots significantly improves the fidelity of phase retrieval. The primary practical limit on phase retrieval via the triple correlations is the computation of the bispectrum which, for a 2D detector, requires storage of a $(N_{\text{pix}} \times N_{\text{pix}})^2$ floating point array. For large detectors, the bispectrum can rapidly consume all available memory on small workstations. The

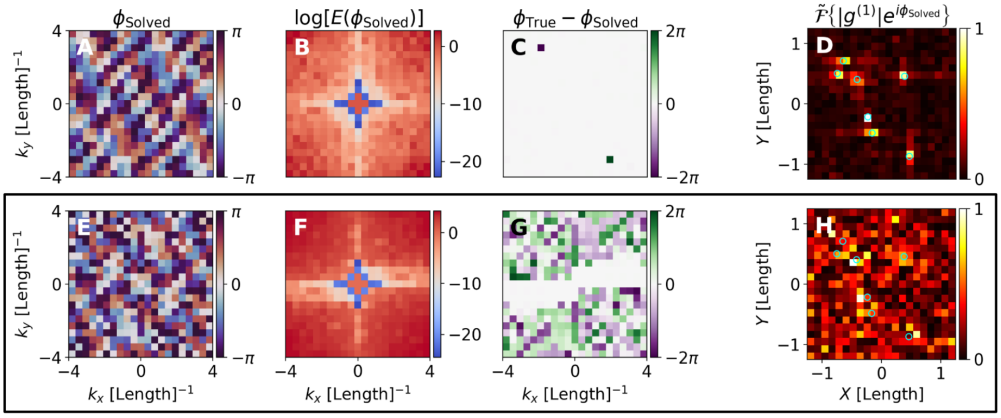


Fig. 4. Exact ab initio phase retrieval from triple correlations both with (A-D) and without (boxed, E-H) alternate value toggling. (A) shows the phase retrieved from the third-order correlations used to produce the object image via Fourier inversion in (D). The true positions of the atoms used in the simulation are indicated by blue points in (D) and (H). (B) shows the error values calculated for each pixel during phase retrieval and (C) shows the difference between the true and retrieved phase values. (E-H) shows the same plots for the same set of atoms and number of shots but without alternate phase value toggling. When alternate phase values at pixels adjacent to spikes in the error function are toggled correctly as in (B), the error is reduced and the difference between the retrieved and true values is small. When alternates are not toggled correctly as in (F), the error is large and faithful structure retrieval is less likely. Phase information past the physical edge of the detector ($\left|\vec{k}_{\text{max}}\right| = 2$ in this example) is retrieved via the triple correlations, enhancing real space resolution.

$11 \times 11$ detector used in the simulation in Figure 4 with $10^4$ shots proved to be a reasonable compromise between memory usage, execution time, and visual impact for purposes of this demonstration when run on a standard laptop computer.

## 5. Conclusions

We have described a mathematical solution to the sign problem in phase retrieval from triple correlations of fluorescent light. We provided a numerical demonstration of our method with simulated data which accurately retrieved the reciprocal space Fourier phase of an atom array. We envision this method as another potential solution to the phase problem in crystallography via photon correlations of fluorescence radiation from atoms pumped by x-ray free-electron lasers. The method presented in this paper may also prove interesting for pulse metrology [14, 15, 30, 31], observing many-body correlations in ultracold atomic gases [32–34], imaging in turbid media [35–37], and for imaging with radio telescope arrays [4–6].

**Funding.** NP acknowledges financial support from the MIT International Science and Technology Initiatives (MISTI) program and the Hertz Foundation.

**Acknowledgments.** NP thanks Anlong Chua for helpful discussions regarding Eq. 25.

**Disclosures.** The authors declare no conflicts of interest.

**Data Availability Statement.** The data and source code which support the results in this paper are available on Github at https://github.com/npeard/CorrSpeck.

**Supplemental document.** See Supplement 1 for supporting content.

## References


1. Y. Shechtman, Y. C. Eldar, O. Cohen, H. N. Chapman, J. Miao, and M. Segev, "Phase retrieval with application to optical imaging: A contemporary overview," IEEE Signal Process. Mag. **32**, 87–109 (2015).
2. R. Twiss, "Applications of intensity interferometry in physics and astronomy," Opt. Acta: Int. J. Opt. **16**, 423–451 (1969).
3. H. Gamo, "Triple correlator of photoelectric fluctuations as a spectroscopic tool," J. Appl. Phys. **34**, 875–876 (1963).
4. P. D. Nuñez and A. Domiciano de Souza, "Capabilities of future intensity interferometers for observing fast-rotating stars: imaging with two- and three-telescope correlations," Mon. Notices Royal Astron. Soc. **453**, 1999–2005 (2015).
5. T. Wentz and P. Saha, "Feasibility of observing hanbury brown and twiss phase," Mon. Notices Royal Astron. Soc. **446**, 2065–2072 (2014).
6. D. Dravins, T. Lagadec, and P. D. Nuñez, "Long-baseline optical intensity interferometry: Laboratory demonstration of diffraction-limited imaging," Astron. & Astrophys. **580**, A99 (2015).
7. V. Malvimat, O. Wucknitz, and P. Saha, "Intensity interferometry with more than two detectors?" Mon. Notices Royal Astron. Soc. **437**, 798–803 (2014).
8. D. Dravins, S. LeBohec, H. Jensen, and P. D. Nuñez, "Optical intensity interferometry with the cherenkov telescope array," Astropart. Phys. **43**, 331–347 (2013).
9. A. Classen, K. Ayyer, H. N. Chapman, R. Röhlsberger, and J. von Zanthier, "Incoherent diffractive imaging via intensity correlations of hard x-rays," Phys. Rev. Lett. **119**, 053401 (2017).
10. R. Schneider, T. Mehringer, G. Mercurio, L. Wenthaus, A. Classen, G. Brenner, O. Gorobtsov, A. Benz, D. Bhatti, L. Bocklage, B. Fischer, S. Lazarev, Y. Obukhov, K. Schlage, P. Skopintsev, J. Wagner, F. Waldmann, S. Willing, I. Zaluzhnyy, W. Wurth, I. A. Vartanyants, R. Röhlsberger, and J. von Zanthier, "Quantum imaging with incoherently scattered light from a free-electron laser," Nat. Phys. **14**, 126–129 (2018).
11. F. Trost, K. Ayyer, and H. N. Chapman, "Photon statistics and signal to noise ratio for incoherent diffraction imaging," New J. Phys. **22**, 083070 (2020).
12. P. J. Ho, C. Knight, and L. Young, "Fluorescence intensity correlation imaging with high spatial resolution and elemental contrast using intense x-ray pulses," Struct. Dyn. **8**, 044101 (2021).
13. L. M. Lohse, M. Vassholz, and T. Salditt, "On incoherent diffractive imaging," Acta Crystallogr. Sect. A Foundations Adv. **77**, 480–496 (2021).
14. I. Inoue, K. Tamasaku, T. Osaka, Y. Inubushi, and M. Yabashi, "Determination of x-ray pulse duration via intensity correlation measurements of x-ray fluorescence," J. Synchrotron Radiat. **26** (2019).
15. N. Nakamura, S. Matsuyama, T. Inoue, I. Inoue, J. Yamada, T. Osaka, M. Yabashi, T. Ishikawa, and K. Yamauchi, "Focus characterization of an x-ray free-electron laser by intensity correlation measurement of x-ray fluorescence," J. Synchrotron Radiat. **27**, 1366–1371 (2020).
16. T. Sato, S. Wadaka, J. Yamamoto, and J. Ishii, "Imaging system using an intensity triple correlator," Appl. Opt. **17**, 2047 (1978).
17. T. Sato, J. Ishii, and S. Wadaka, "Computer controlled image sensor and its application," Appl. Opt. **18**, 485 (1979).
18. T. Sato, K. Sasaki, and K. Ando, "Adaptive techniques for precise detection of the coherence function by an intensity triple correlator," Appl. Opt. **20**, 2055 (1981).
19. P. Fontana, "Multidetector intensity interferometers," J. Appl. Phys. **54** (1983).
20. A. W. Lohmann, G. Weigelt, and B. Wirnitzer, "Speckle masking in astronomy: triple correlation theory and applications," Appl. Opt. **22**, 4028 (1983).
21. A. W. Lohmann and B. Wirnitzer, "Triple correlations," Proc. IEEE **72** (1984).
22. H. Bartelt, A. W. Lohmann, and B. Wirnitzer, "Phase and amplitude recovery from bispectra," Appl. Opt. **23**, 3121 (1984).
23. T. Matsuoka and T. Ulrych, "Phase estimation using the bispectrum," Proc. IEEE **72**, 1403–1411 (1984).
24. J. E. Baldwin, C. A. Haniff, C. D. Mackay, and P. J. Warner, "Closure phase in high-resolution optical imaging," Nature **320**, 595–597 (1986).
25. J. I. Yellott and G. J. Iverson, "Uniqueness properties of higher-order autocorrelation functions," J. Opt. Soc. Am. A **9**, 388 (1992).
26. A. S. Marathay, Y. Hu, and L. Shao, "Phase function of spatial coherence from second-, third-, and fourth- order intensity correlations," Opt. Eng. **33**, 3265 (1994).
27. E. Sayrol, C. Nikias, and A. Gasull, "Image restoration using the w-slice method," IEEE Transactions on Image Process. **4**, 1174–1181 (1995).
28. R. Holambe, A. Ray, and T. Basu, "Signal phase recovery using the bispectrum," Signal Process. **55**, 321–337 (1996).
29. G. Shoulga and E. N. Ribak, "Toward spectral intensity interferometry," Appl. Opt. **56**, A23 (2017).
30. T. Feurer, S. Niedermeier, and R. Sauerbrey, "Measuring the temporal intensity of ultrashort laser pulses by triple correlation," Appl. Phys. B: Lasers Opt. **66**, 163–168 (1998).
31. T.-M. Liu, Y.-C. Huang, G.-W. Chern, K.-H. Lin, C.-J. Lee, Y.-C. Hung, and C.-K. Sun, "Triple-optical autocorrelation for direct optical pulse-shape measurement," Appl. Phys. Lett. **81**, 1402–1404 (2002).
32. S. Fölling, F. Gerbier, A. Widera, O. Mandel, T. Gericke, and I. Bloch, "Spatial quantum noise interferometry in expanding ultracold atom clouds," Nature **434**, 11 (2005).
33. T. Jeltes, J. M. McNamara, W. Hogervorst, W. Vassen, V. Krachmalnicoff, M. Schellekens, A. Perrin, H. Chang, D. Boiron, A. Aspect, and C. I. Westbrook, "Comparison of the hanbury brown–twiss effect for bosons and fermions,"

Nature **445**, 402–405 (2007).
34. M. R. Andrews, C. Townsend, H. Miesner, D. Durfee, D. Kurn, and W. Ketterle, "Observation of interference between two bose condensates," Science **275**, 637–641 (1997).
35. J. Bertolotti, E. G. van Putten, C. Blum, A. Lagendijk, W. L. Vos, and A. P. Mosk, "Non-invasive imaging through opaque scattering layers," Nature **491**, 232–234 (2012).
36. O. Katz, P. Heidmann, M. Fink, and S. Gigan, "Non-invasive single-shot imaging through scattering layers and around corners via speckle correlations," Nat. Photonics **8**, 784–790 (2014).
37. G. Stern and O. Katz, "Non-invasive focusing through scattering layers using speckle-correlations," Opt. Lett. **44**, 143 (2019). ArXiv: 1808.03267.
38. R. J. Glauber, "Photon correlations," Phys. Rev. Lett. **10**, 84–86 (1963).
39. R. J. Glauber, "The quantum theory of optical coherence," Phys. Rev. **130**, 2529–2539 (1963).
40. R. J. Glauber, "Coherent and incoherent states of the radiation field," Phys. Rev. **131**, 2766–2788 (1963).
41. J. Peřina, *Quantum Statistics of Linear and Nonlinear Optical Phenomena* (Springer Netherlands, 1991), 2nd ed.
42. V. A. Mandelshtam and H. S. Taylor, "Harmonic inversion of time signals and its applications," The J. Chem. Phys. **107**, 6756–6769 (1997).
43. V. A. Mandelshtam and H. S. Taylor, "Multidimensional harmonic inversion by filter-diagonalization," The J. Chem. Phys. **108**, 9970–9977 (1998).
44. V. A. Mandelshtam, "On harmonic inversion of cross-correlation functions by the filter diagonalization method," J. Theor. Comput. Chem. **02**, 497–505 (2003).

## 6. Appendix

### 6.1. Importance of the Fourier Phase

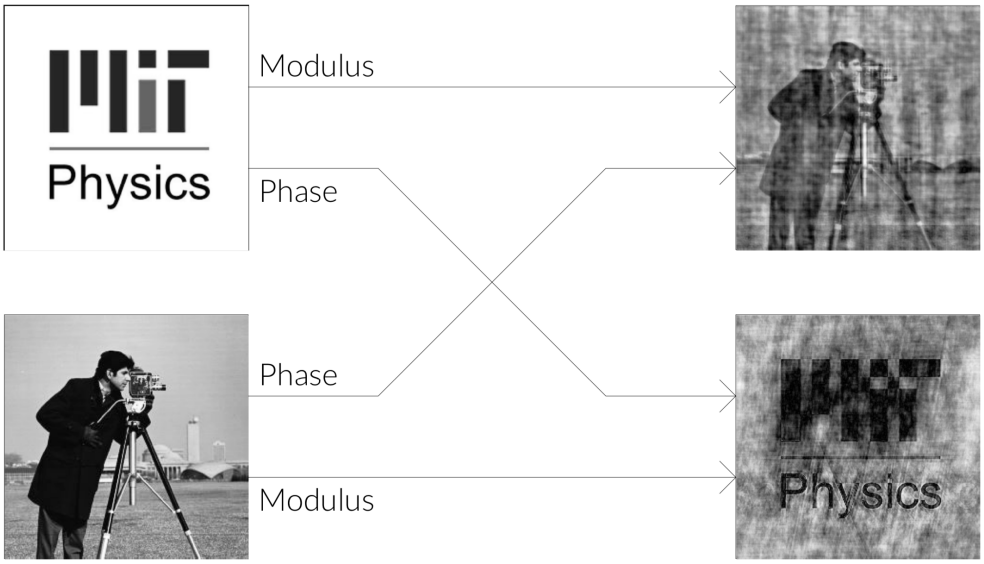


Fig. 5. Two images (left) are Fourier transformed. Swapping the phases of the transformed images and then executing the inverse Fourier transform (right) demonstrates the importance of the phase information in diffractive imaging. Square-law detectors (most photodetectors) cannot access the phase of the light field directly, so creative indirect techniques are required to recover the total light field.

### 6.2. Detection of a Photon

The reader may wish to refer to [38–41] in the next few sections where we derive the expression for intensity triple correlations used in the main text.

Consider some initial state of the photon field $|i\rangle$ with some detection device in the ground state. $|f\rangle$ is the final state of the field after our detection system has been excited by a photon. The transition amplitude for this event is then

$$A = \langle f | \hat{\psi} | i \rangle \tag{26}$$

and the transition probability is

$$P = |A|^2 = \left| \langle f | \hat{\psi} | i \rangle \right|^2 \tag{27}$$

where $\psi$ is the photon field annihilation operator. The final state of the field is usually not observed directly, so we trace over the possible $|f\rangle$

$$P = \sum_f \langle i | \hat{\psi}^\dagger | f \rangle \langle f | \hat{\psi} | i \rangle = \langle i | \hat{\psi}^\dagger \hat{\psi} | i \rangle \tag{28}$$

This short calculation shows how photon detection is analogous to a measurement of the degree of first-order coherence.

### 6.3. First-Order Coherence in Diffraction

In coherent diffraction experiments, we measure the degree of first-order coherence as a function of reciprocal space.

$$G^{(1)}(\vec{k}) = \langle \hat{\Psi}^{\dagger}(\vec{k})\hat{\Psi}(\vec{0})\rangle \tag{29}$$

where $\hat{\Psi}(k) = \sum_i^{\nu} e^{-i\vec{k}\cdot\vec{r}_i}\hat{a}_i$ is the photon field operator summing over the number of emitters ($\nu$) and the first-order correlation function measures the coherence of a scattered wave ($\vec{k}$) relative to the incident wave ($\vec{0}$).

$$G^{(1)}(\vec{k}) = \sum_{ij}^{\nu} e^{i\vec{k}\cdot\vec{r}_i}\langle \hat{a}_i^{\dagger}\hat{a}_j\rangle \tag{30}$$

For elastic scattering, we can generally regard the state of the light field to be classical and that the scattered wave from each atom has the same intensity

$$G^{(1)}(\vec{k}) = \sum_{ij}^{\nu} e^{i\vec{k}\cdot\vec{r}_i}\alpha_i^*\alpha_j \tag{31}$$

and $\alpha_i = \alpha_j = \alpha$

$$G^{(1)}(\vec{k}) = |\alpha|^2\,\nu\sum_{j}^{\nu} e^{i\vec{k}\cdot\vec{r}_j} \tag{32}$$

It follows that $G(0) = |\alpha|^2\,\nu^2$ so the normalized correlation function is

$$g^{(1)}(\vec{k}) = \frac{G^{(1)}(\vec{k})}{G^{(1)}(\vec{0})} = \frac{1}{\nu}\sum_{j}^{\nu} e^{i\vec{k}\cdot\vec{r}_j} \tag{33}$$

Square-law detectors measure only the fringe visibility, eliminating the phase information of the first-order coherence

$$\left|g^{(1)}(\vec{k})\right|^2 = \frac{1}{\nu^2}\left|\sum_{j}^{\nu} e^{i\vec{k}\cdot\vec{r}_j}\right|^2 \tag{34}$$

### 6.4. Pair Correlation Function

Light with no first-order coherence (e.g., fluorescence) can still exhibit second-order coherence. The pair-wise correlation function is written in second-quantization as

$$G^{(2)}(\vec{k}_1,\vec{k}_2) = \langle \hat{\psi}^{\dagger}(\vec{k}_1)\hat{\psi}^{\dagger}(\vec{k}_2)\hat{\psi}(\vec{k}_1)\hat{\psi}(\vec{k}_2)\rangle \tag{35}$$

where the angle brackets indicate the expectation value of a quantum state. Expanding single-particle states in a single mode of momentum-space

$$\hat{\psi}(\vec{k}) = \sum_{i}^{\nu} e^{-i\vec{k}\cdot\vec{r}_i}e^{-i\phi_i}\hat{a}_i = \sum_{i}^{\nu}\mathcal{E}_i(\vec{k})\hat{a}_i \tag{36}$$

with $\phi_i \in [0, 2\pi)$ a random phase that varies slower than the coherence time. In this picture, each atom at $\vec{r}_i$ emits a photon into the mode $\vec{k}$ with phase $\phi_i$.

The pair-wise correlation averaged over an ensemble of measurements (shots) is

$$\left\{G^{(2)}(\vec{k}_1,\vec{k}_2)\right\} = \left\{\sum_{ijkl}^{\nu}\mathcal{E}_i^*(\vec{k}_1)\mathcal{E}_j^*(\vec{k}_2)\mathcal{E}_k(\vec{k}_1)\mathcal{E}_l(\vec{k}_2)\langle \hat{a}_i^{\dagger}\hat{a}_j^{\dagger}\hat{a}_k\hat{a}_l\rangle\right\} \tag{37}$$

The outer braces notate the ensemble mean.

There are two cases where the ensemble mean pair-wise correlation is non-zero:

$$i = k, \quad j = l \tag{38}$$

$$i = l, \quad j = k \tag{39}$$

We contract the fields accordingly and rewrite the correlation function as

$$\begin{aligned}\left\{G^{(2)}(\vec{k}_1, \vec{k}_2)\right\} = \\ &\left\{ \sum_{ij}^{\nu} \mathcal{E}_i^*(\vec{k}_1)\mathcal{E}_j^*(\vec{k}_2)\mathcal{E}_i(\vec{k}_1)\mathcal{E}_j(\vec{k}_2)\langle \hat{a}_i^\dagger \hat{a}_j^\dagger \hat{a}_i \hat{a}_j \rangle \right. \\ &+ \mathcal{E}_i^*(\vec{k}_1)\mathcal{E}_j^*(\vec{k}_2)\mathcal{E}_j(\vec{k}_1)\mathcal{E}_i(\vec{k}_2)\langle \hat{a}_i^\dagger \hat{a}_j^\dagger \hat{a}_j \hat{a}_i \rangle \\ &\left. - \sum_{i}^{\nu} \mathcal{E}_i^*(\vec{k}_1)\mathcal{E}_i^*(\vec{k}_2)\mathcal{E}_i(\vec{k}_1)\mathcal{E}_i(\vec{k}_2)\langle \hat{a}_i^\dagger \hat{a}_i^\dagger \hat{a}_i \hat{a}_i \rangle \right\}\end{aligned} \tag{40}$$

By writing out the first two terms with $i, j$ indices over the number of emitters we double count the case that $i = j$. In Equation 40, we have subtracted this case once in the last term.

The quantum-classical correspondence between field annihilation/creation operators and classical waves ($\hat{A}^{(+)} \leftrightarrow V$ and $\hat{A}^{(-)} \leftrightarrow V^*$) with normal ordered correlation functions is implemented with the use of the coherent states $|\{\alpha\}\rangle$ [41]. Fock states have no corresponding classical state and must be treated separately.

#### 6.4.1. Classical Light

Consider the case that each atom emits a single coherent field so that the initial state of the field is

$$|\{\alpha\}\rangle = \prod_{\lambda}^{\nu} |\alpha_\lambda\rangle \tag{41}$$

$$\hat{a}_\sigma |\{\alpha\}\rangle = \alpha_\sigma |\{\alpha\}\rangle \tag{42}$$

where $|\alpha_\lambda\rangle$ is the state contributed by the $\lambda$th atom. Note that

$$\langle\{\alpha\}| \hat{a}_\mu^\dagger \hat{a}_\sigma |\{\alpha\}\rangle = \alpha_\mu^* \alpha_\sigma \tag{43}$$

since the coherent states are eigenstates of $\hat{a}$. Because the correlation function operator is normal ordered, we can directly resume from Equation 40 with

$$\begin{aligned}\left\{G^{(2)}(\vec{k}_1, \vec{k}_2)\right\} = &\left\{ \sum_{ij}^{\nu} \mathcal{E}_i^*(\vec{k}_1)\mathcal{E}_j^*(\vec{k}_2)\mathcal{E}_i(\vec{k}_1)\mathcal{E}_j(\vec{k}_2) |\alpha_i|^2 |\alpha_j|^2 \right. \\ &\left. + \mathcal{E}_i^*(\vec{k}_1)\mathcal{E}_j^*(\vec{k}_2)\mathcal{E}_j(\vec{k}_1)\mathcal{E}_i(\vec{k}_2) |\alpha_i|^2 |\alpha_j|^2 - \sum_{i}^{\nu} \mathcal{E}_i^*(\vec{k}_1)\mathcal{E}_i^*(\vec{k}_2)\mathcal{E}_i(\vec{k}_1)\mathcal{E}_i(\vec{k}_2) |\alpha_i|^4 \right\}\end{aligned} \tag{44}$$

Now, the ensemble cancellation of random phases in the $\mathcal{E}_i(k)$ gives the following approximation

$$\begin{aligned}N\left\{G^{(2)}(\vec{k}_1, \vec{k}_2)\right\} \approx &\sum_{ij}^{\nu} \left|\mathcal{E}_i(\vec{k}_1)\right|^2 \left|\mathcal{E}_j(\vec{k}_2)\right|^2 |\alpha_i|^2 |\alpha_j|^2 \\ &+ \mathcal{E}_i^*(\vec{k}_1)\mathcal{E}_j^*(\vec{k}_2)\mathcal{E}_j(\vec{k}_1)\mathcal{E}_i(\vec{k}_2) |\alpha_i|^2 |\alpha_j|^2 - \sum_{i}^{\nu} \left|\mathcal{E}_i(\vec{k}_1)\right|^4 |\alpha_i|^4\end{aligned} \tag{45}$$

Supposing identical emission from each atom, $\alpha_i = \alpha_j = \alpha$, and recalling $|\mathcal{E}_i(k)|^2 = 1$, we can reduce the sums over constant terms

$$N\left\{G^{(2)}(\vec{k}_1, \vec{k}_2)\right\} \approx \nu^2 |\alpha|^4 - \nu |\alpha|^4 + \sum_{ij}^{\nu} \mathcal{E}_i^*(\vec{k}_1)\mathcal{E}_j^*(\vec{k}_2)\mathcal{E}_j(\vec{k}_1)\mathcal{E}_i(\vec{k}_2) |\alpha|^4 \tag{46}$$

We can rewrite the last term

$$\sum_{ij}^{\nu} \mathcal{E}_i^*(\vec{k}_1)\mathcal{E}_i(\vec{k}_2)\mathcal{E}_j^*(\vec{k}_2)\mathcal{E}_j(\vec{k}_1) = \sum_{ij}^{\nu} e^{i(\vec{k}_1 - \vec{k}_2)\cdot\vec{r}_j} e^{-i(\vec{k}_1 - \vec{k}_2)\cdot\vec{r}_i} = \left|\sum_{j}^{\nu} e^{i\vec{q}\cdot\vec{r}_j}\right|^2 \tag{47}$$

where $\vec{q} = \vec{k}_1 - \vec{k}_2$. Normalizing the entire correlation function by dividing out the square of

$$N\left\{\langle\hat{\psi}^\dagger(\vec{0})\hat{\psi}(\vec{0})\rangle\right\} = N\left\{\sum_{ij}^{\nu} e^{i(\phi_i - \phi_j)}\langle\hat{a}_i^\dagger\hat{a}_j\rangle\right\} \approx \sum_{ij}^{\nu}\langle\hat{a}_i^\dagger\hat{a}_j\rangle\delta_{ij} = \sum_{i}^{\nu}\langle\hat{a}_i^\dagger\hat{a}_i\rangle = \nu |\alpha|^2 \tag{48}$$

we can express the normalized second-order correlation function

$$g^{(2)}(\vec{k}_1, \vec{k}_2) = \frac{\left\{G^{(2)}(\vec{k}_1, \vec{k}_2)\right\}}{\left\{\hat{\psi}^\dagger(\vec{0})\hat{\psi}(\vec{0})\right\}^2} \tag{49}$$

as

$$g^{(2)}(\vec{k}_1, \vec{k}_2) \approx 1 - \frac{1}{\nu} + \frac{1}{\nu^2}\left|\sum_{j}^{\nu} e^{i\vec{q}\cdot\vec{r}_j}\right|^2 \tag{50}$$

Observe that the last term is identical to the modulus square first-order correlation function from Equation 34. Apparently, the coherent diffraction pattern is recovered from photon pair correlations of fluorescence speckle intensities.

$$g^{(2)}(\vec{k}_1, \vec{k}_2) \approx 1 - \frac{1}{\nu} + \left|g^{(1)}(\vec{q})\right|^2 \tag{51}$$

The imperfect cancellation of random phases causes the "phase noise" of Hanbury Brown and Twiss. The more atoms included, the longer random walk in the complex plane requires additional shots to reach the same level of phase noise as with fewer atoms.

### 6.4.2. Quantum Light

Consider the case that each atom emits a single photon so that the initial state of the field is defined

$$|\{n\}\rangle = \prod_{\lambda}^{\nu} |n_\lambda\rangle \tag{52}$$

$$\hat{a}_\sigma |\{n\}\rangle = \sqrt{n_\sigma}\,|\{n_1, n_2, ..., n_\sigma - 1, n_{\sigma+1}, ...\}\rangle \tag{53}$$

where $|n_\lambda\rangle$ is the state contributed by the $\lambda$th atom. Note that

$$\langle\{n\}|\,\hat{a}_\mu^\dagger\hat{a}_\sigma\,|\{n\}\rangle = \sqrt{n_\mu}\sqrt{n_\sigma}\delta_{\mu\sigma} \tag{54}$$

requires an exact match of creation and annihilation operator indices to be non-zero, since Fock states form an orthonormal basis and are not eigenstates of $\hat{a}$ or $\hat{a}^\dagger$.

For coherent states, the normal-ordered correlation operator is already diagonalized. For Fock states, this is not so. The commutation relation $[\hat{a}_i, \hat{a}_j^\dagger] = \delta_{ij}$ allows us to diagonalize the cases 38 and 39

$$\langle \hat{a}_i^\dagger \hat{a}_j^\dagger \hat{a}_i \hat{a}_j \rangle = \langle \hat{a}_i^\dagger \hat{a}_i \hat{a}_j^\dagger \hat{a}_j \rangle - \langle \hat{a}_i^\dagger \hat{a}_j \delta_{ij} \rangle \tag{55}$$

$$\langle \hat{a}_i^\dagger \hat{a}_j^\dagger \hat{a}_j \hat{a}_i \rangle = \langle \hat{a}_j^\dagger \hat{a}_j \hat{a}_i^\dagger \hat{a}_i \rangle - \langle \hat{a}_j^\dagger \hat{a}_i \delta_{ij} \rangle \tag{56}$$

as well as the double-counting correction term in 40

$$\langle \hat{a}_i^\dagger \hat{a}_i^\dagger \hat{a}_i \hat{a}_i \rangle = \langle \hat{a}_i^\dagger \hat{a}_i \hat{a}_i^\dagger \hat{a}_i \rangle - \langle \hat{a}_i^\dagger \hat{a}_i \rangle \tag{57}$$

Writing the expectation value $\langle \hat{a}_i^\dagger \hat{a}_i \rangle = n_i$ as the occupation number of the mode emitted by the $i$th atom, the diagonalized second order correlation function (Eq. 40) reads

$$\left\{ G^{(2)}(\vec{k}_1, \vec{k}_2) \right\} = \left\{ \sum_{ij}^{\nu} n_i n_j \left| \mathcal{E}_i(\vec{k}_1) \right|^2 \left| \mathcal{E}_j(\vec{k}_2) \right|^2 + \right.$$
$$\left. n_i n_j \mathcal{E}_i^*(\vec{k}_1) \mathcal{E}_i(\vec{k}_2) \mathcal{E}_j^*(\vec{k}_2) \mathcal{E}_j(\vec{k}_1) - \sum_{i}^{\nu} n_i^2 \left| \mathcal{E}_i(\vec{k}_1) \right|^4 - \sum_{i}^{\nu} n_i \left| \mathcal{E}_i(\vec{k}_1) \right|^4 \right\} \tag{58}$$

Supposing single photon emission from identical atoms, $n_i = n_j = 1$ and writing $\left| \mathcal{E}_j(k_2) \right|^2 = 1$, we get

$$\left\{ G^{(2)}(\vec{k}_1, \vec{k}_2) \right\} = \left\{ \nu^2 - 2\nu + \sum_{ij}^{\nu} \mathcal{E}_i^*(\vec{k}_1) \mathcal{E}_i(\vec{k}_2) \mathcal{E}_j^*(\vec{k}_2) \mathcal{E}_j(\vec{k}_1) \right\} \tag{59}$$

Normalizing by $\left\{ \hat{\psi}^\dagger(\vec{0}) \hat{\psi}(\vec{0}) \right\}^2 = \nu^2$ as in the previous section, we obtain

$$g^{(2)}(\vec{k}_1, \vec{k}_2) = 1 - \frac{2}{\nu} + \left| g^{(1)}(\vec{q}) \right|^2 \tag{60}$$

which is quite similar to the case where we assume classical light. Note here, however, that the expression is an exact equality - this is due to the orthogonality of Fock states contracting only those random phases which cancel perfectly. There are no $\left\{ e^{i\phi_i} e^{-i\phi_j} \right\}$ terms where $i \neq j$, so the ensemble average over shots is not subject to the Hanbury Brown and Twiss phase noise.

### *6.5. Triple Correlation Function*

The correlation function between triples of photons is written in second-quantization as

$$G^{(3)}(\vec{k}_1, \vec{k}_2, \vec{k}_3) = \langle \hat{\psi}^\dagger(\vec{k}_1) \hat{\psi}^\dagger(\vec{k}_2) \hat{\psi}^\dagger(\vec{k}_3) \hat{\psi}(\vec{k}_1) \hat{\psi}(\vec{k}_2) \hat{\psi}(\vec{k}_3) \rangle \tag{61}$$

where the field operators are defined as before. The triple correlation averaged over an ensemble of measurements is

$$\left\{ G^{(3)}(\vec{k}_1, \vec{k}_2, \vec{k}_3) \right\} = \left\{ \sum_{ijklmn}^{\nu} \mathcal{E}_i^*(\vec{k}_1) \mathcal{E}_j^*(\vec{k}_2) \mathcal{E}_k^*(\vec{k}_3) \mathcal{E}_l(\vec{k}_1) \mathcal{E}_m(\vec{k}_2) \mathcal{E}_n(\vec{k}_3) \langle \hat{a}_i^\dagger \hat{a}_j^\dagger \hat{a}_k^\dagger \hat{a}_l \hat{a}_m \hat{a}_n \rangle \right\} \tag{62}$$

and again we must consider the field contractions for which the expression is non-zero. We find that there are six

$$i = l, \quad j = m, \quad k = n \tag{63}$$

$$i = n, \quad j = l, \quad k = m \tag{64}$$

$$i = m, \quad j = n, \quad k = l \tag{65}$$

$$i = l, \quad j = n, \quad k = m \tag{66}$$

$$i = n, \quad j = m, \quad k = l \tag{67}$$

$$i = m, \quad j = l, \quad k = n \tag{68}$$

The first case (63) contracts fields with the same $\vec{k}$, and will thus be a constant after summation and averaging. For the remaining cases, we must carefully account for double- and triple-counting. We can quickly see that cases 66, 67, and 68 each contract one set of fields with the same $\vec{k}$, leaving a pair of free indices which do not contract to a constant. Each of these pairs over count 63 when the indices are equal, so we must subtract this case from each of 66, 67, and 68. The cases 64 and 65, however, have three free indices which do not produce field contractions to a constant. Firstly, we can contract any pair of the three indices in each of 64 and 65 to get the result of any one of 66, 67, and 68 again - this over counts each of 66, 67, and 68 once for each of 64 and 65. Additionally, this overcounting correction must itself be corrected just as 66, 67, and 68 were above. Finally, 64 and 65 each overcount the case where all three indices are equal. All cases (63 through 68) over-counting corrections can be expressed as

$$\begin{aligned}
&\delta_{il}\delta_{jm}\delta_{kn} \\
&+\delta_{in}\delta_{jl}\delta_{km}\left(1-\delta_{ij}\right)\left(1-\delta_{jk}\right)\left(1-\delta_{ki}\right) \\
&+\delta_{im}\delta_{jn}\delta_{kl}\left(1-\delta_{ij}\right)\left(1-\delta_{jk}\right)\left(1-\delta_{ki}\right) \\
&+\delta_{il}\delta_{jn}\delta_{km}\left(1-\delta_{jk}\right) \\
&+\delta_{in}\delta_{jm}\delta_{kl}\left(1-\delta_{ki}\right) \\
&+\delta_{im}\delta_{jl}\delta_{kn}\left(1-\delta_{ij}\right) \\
&= \delta_{il}\delta_{jm}\delta_{kn} \\
&+\delta_{in}\delta_{jl}\delta_{km}(1-\delta_{ij}-\delta_{jk}-\delta_{ki}+\delta_{ij}\delta_{jk}+\delta_{jk}\delta_{ki}+\delta_{ki}\delta_{ij}-\delta_{ij}\delta_{jk}\delta_{ki}) \\
&+\delta_{im}\delta_{jn}\delta_{kl}(1-\delta_{ij}-\delta_{jk}-\delta_{ki}+\delta_{ij}\delta_{jk}+\delta_{jk}\delta_{ki}+\delta_{ki}\delta_{ij}-\delta_{ij}\delta_{jk}\delta_{ki}) \\
&+\delta_{il}\delta_{jn}\delta_{km}\left(1-\delta_{jk}\right) \\
&+\delta_{in}\delta_{jm}\delta_{kl}\left(1-\delta_{ki}\right) \\
&+\delta_{im}\delta_{jl}\delta_{kn}\left(1-\delta_{ij}\right)
\end{aligned} \tag{69}$$

when contracted with the six-fold sum 62.

#### 6.5.1. Classical Light

Consider once more our scenario where classical light is emitted

$$|\{\alpha\}\rangle = \prod_{\lambda}^{\nu} |\alpha_\lambda\rangle \tag{70}$$

As with the pair correlation operator above, the triple correlation operator is diagonal in the coherent state basis. Proceeding analogously and defining

$$\vec{q}_1 = \vec{k}_1 - \vec{k}_2 \tag{71}$$

$$\vec{q}_2 = \vec{k}_2 - \vec{k}_3 \tag{72}$$

$$\vec{q}_3 = \vec{k}_3 - \vec{k}_1 = -\vec{q}_1 - \vec{q}_2 \tag{73}$$

we soon reach the expression

$$N\left\{G^{(3)}(\vec{k}_1,\vec{k}_2,\vec{k}_3)\right\} \approx \left(\nu^3-3\nu^2+4\nu\right)|\alpha|^6 + (\nu-2)\left(\left|\sum_j^\nu |\alpha|^3\, e^{i\vec{q}_1\cdot\vec{r}_j}\right|^2 + \left|\sum_j^\nu |\alpha|^3\, e^{i\vec{q}_2\cdot\vec{r}_j}\right|^2 + \left|\sum_j^\nu |\alpha|^3\, e^{i\vec{q}_3\cdot\vec{r}_j}\right|^2\right) + |\alpha|^6\sum_{ijk} e^{i\vec{q}_1\cdot\vec{r}_i}e^{i\vec{q}_2\cdot\vec{r}_j}e^{i\vec{q}_3\cdot\vec{r}_k} + |\alpha|^6\sum_{ijk} e^{-i\vec{q}_1\cdot\vec{r}_i}e^{-i\vec{q}_2\cdot\vec{r}_j}e^{-i\vec{q}_3\cdot\vec{r}_k} \quad (74)$$

remembering the over-counting rules from the previous section. Observe that the last two terms are products of independent sums and complex conjugates. Moreover, each of the second, third, and fourth terms is a first-order correlation function 32. After normalizing by the cube of $|\alpha|^2\,\nu$, we write

$$g^{(3)}(\vec{k}_1,\vec{k}_2,\vec{k}_3) = \left(1-\frac{3}{\nu}+\frac{4}{\nu^2}\right)+\left(1-\frac{2}{\nu}\right)\left(\left|g^{(1)}(\vec{q}_1)\right|^2+\left|g^{(1)}(\vec{q}_2)\right|^2+\left|g^{(1)}(\vec{q}_3)\right|^2\right) + 2\mathrm{Re}\left(g^{(1)}(\vec{q}_1)g^{(1)}(\vec{q}_2)g^{(1)}(\vec{q}_3)\right) \quad (75)$$

The last term here is the subject of the main text and allows retrieval of the exact structural phase $\phi(\vec{q})$ sought in coherent diffraction experiments.

#### 6.5.2. Quantum Light

As with the pair correlations of quantum light, the triple correlator acting on non-classical states of the field picks up additional corrections during diagonalization. There are six terms (neglecting the over-counting correction terms, which must also be diagonalized) that must be diagonalized in the Fock basis. As an example, diagonalizing the first term of 69 produces the operator

$$\langle \hat{a}_i^\dagger\hat{a}_j^\dagger\hat{a}_k^\dagger\hat{a}_i\hat{a}_j\hat{a}_k\rangle = \langle \hat{a}_i^\dagger\hat{a}_i\hat{a}_j^\dagger\hat{a}_j\hat{a}_k^\dagger\hat{a}_k - \hat{a}_i^\dagger\hat{a}_i\hat{a}_j^\dagger\hat{a}_k\delta_{jk} - \hat{a}_i^\dagger\hat{a}_j\hat{a}_k^\dagger\hat{a}_k\delta_{ij} + \hat{a}_i^\dagger\hat{a}_k\delta_{ij}\delta_{kj} - \hat{a}_i^\dagger\hat{a}_k\hat{a}_j^\dagger\hat{a}_j\delta_{ik} + \hat{a}_i^\dagger\hat{a}_j\delta_{ik}\delta_{jk}\rangle \quad (76)$$

Clearly, obtaining the exact form of the triple correlations for chaotic quantum light is a tedious task. The result is not important for this paper, but it is important to realize that the classical and quantum cases lead to different expressions. We will skip this derivation for now.

### *6.6. Friedel's Law and Symmetries of $\Phi(\vec{m},\vec{n})$*

Given a real function $f(x)$, its Fourier Transform $F(k) = \mathcal{F}(f(x))$ has the following properties:

$$F(k) = F^*(-k) \quad (77)$$

$$|F(k)|^2 = |F(-k)|^2 \quad (78)$$

For $\phi(k) = \arg(F(k))$,

$$\phi(-k) = -\phi(k) \quad (79)$$

leads to some useful symmetries of the correlation functions and phase map

$$g^{(1)}(x) = g^{(1)*}(-x) \quad (80)$$

$$\Phi(m,n) = \Phi(n,m) \quad (81)$$

$$\Phi(0,n) = \Phi(m,0) = 0 \quad (82)$$

$$\Phi(m,n) = \Phi(-n,-m) \quad (83)$$

$$\Phi(-m,m) = 0 \quad (84)$$

### 6.7. *Coherent Scattering Pattern Retrieval*

Figure 6 shows the result of calculating the pairwise correlation function $g^{(2)}(\vec{q})$ from first-order incoherent fluorescence of atoms. The autocorrelation enables accurate retrieval of the coherent scattering pattern out to $2|\vec{k}_{\max}|$ (past the physical edge of the detector at $|\vec{k}_{\max}|$) [11].

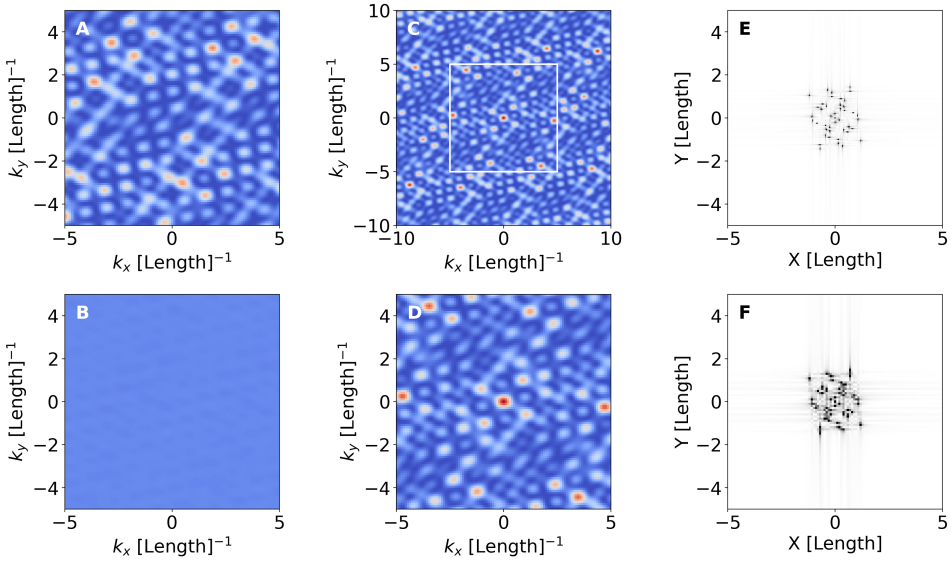


Fig. 6. Simulated fluorescence from a 2D array of seven classical point sources. (A) shows a speckle pattern, representing a single (random) phase relationship between point sources. (B) shows the mean of 1000 speckle patterns with the atom phases changing between shots. The result has nearly zero contrast. The sum of second-order (auto)correlations of the same shots (C) contains the coherent diffraction pattern (D) in the boxed region of (C) plus extra coherent diffraction data beyond the maximum scattering angle covered by the detector. The augmented k-space window produces a real space (object) autocorrelation function with enhanced spatial resolution (E) compared to the real space autocorrelation (F) obtained from inverse Fourier inversion of (C) and (D).

### 6.8. *Extended Momentum Space Sampling Enhances Real Space Resolution*

Figure 7 shows that extended sampling of momentum space enhances the resolution of the real space autocorrelation and, if the phase information is available, the resolution of inverse Fourier Transform of the scattered light (the object).

### 6.9. *The Cross-Correlation Theorem*

For correlations of one-dimensional or small two-dimensional pixel arrays, computationally, it is usually faster to work directly with the outer product of the arrays, sum the resulting matrix along the diagonal, and divide out the underlying support (which represents correlations of unbunched photons). However, for larger arrays, this computation rapidly becomes memory-limited; for example, the second-order correlation of a typical 1000 by 1000 pixel array involves the calculation of a four-dimensional array represented by $1000^4$ floating point numbers. If each floating point number were 32 bits, we would need about 4 terabytes to store this array.

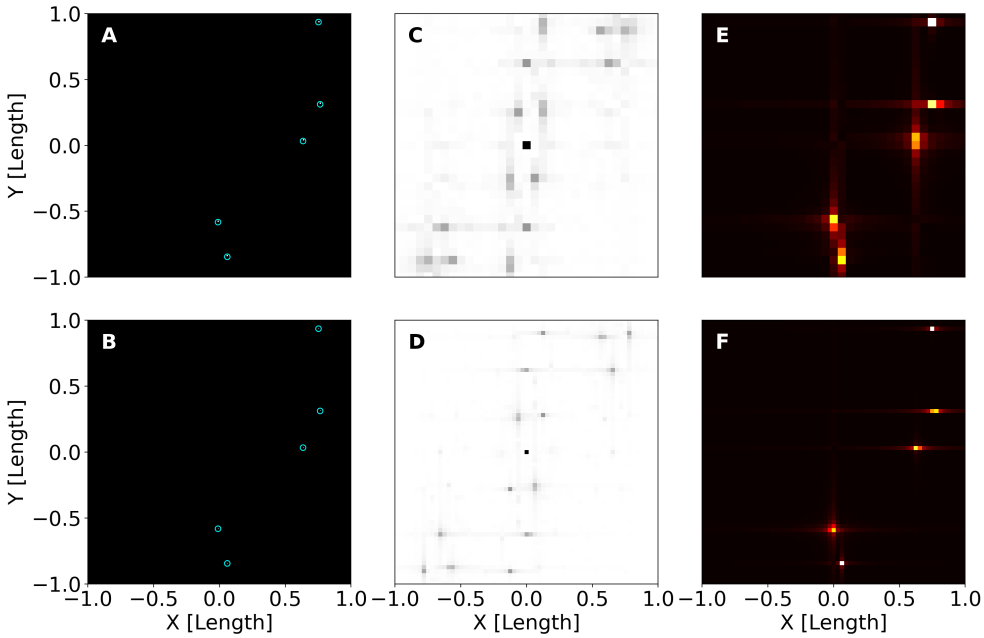


Fig. 7. (A) and (B) show the same array of atoms. (B) has double the spatial resolution (localization) of (A). The inverse Fourier Transform of simulated coherent scatter (C) and (D) retrieves only the real space autocorrelation of the array since the phase information has been lost. In (E) and (F), the phase information is added back to break the translational symmetry and arrive at the original array. Note that in (D) and (F), where the simulated coherent scatter goes out to $2\left|\vec{k}_{\max}\right|$, it is possible to resolve nearby atoms with much greater visibility than in (C) and (E), in which only data out to $\left|\vec{k}_{\max}\right|$ in momentum space is used.

The Cross-Correlation Theorem provides a simple method to calculate correlations using the Fast Fourier Transform. Let $f \bigstar g$ denote the cross correlation of $f(x)$ and $g(x)$. The Cross-Correlation Theorem states

$$f \bigstar g = \mathcal{F}^{-1}[F(k)G^*(k)] \tag{85}$$

where $\mathcal{F}^{-1}$ indicates the inverse Fourier transform and $F(k)$ and $G(k)$ are the Fourier transforms of $f(x)$ and $g(x)$. If $f$ and $g$ are real-valued then

$$f \bigstar g = \mathcal{F}^{-1}[F(k)G(-k)] = f(x) * g(-x) \tag{86}$$

The autocorrelation $G^{(2)}(k_1, k_2)$ of intensities $I(k)$ on a detector is then

$$G^{(2)}(k_1 - k_2) = I(k_1) \bigstar I(k_2) = I(k_1) * I(-k_2) \tag{87}$$

where the last expression is the convolution of intensities.

The triple correlation

$$G^{(3)}(k_1, k_2, k_3) = I(k_1) \bigstar I(k_2) \bigstar I(k_3) \tag{88}$$

is most easily calculated from the bispectrum as

$$G^{(3)}(q_1, q_2) = \mathcal{F}^{-1}[\tilde{I}(u)\tilde{I}(v)\tilde{I}(-u - v)] \tag{89}$$

where $u = k_1 - k_2$ and $v = k_2 - k_3$.

### 6.10. Coarse Binning and Interpolation of Phase Information

A major difficulty of performing a triple correlation experiment is the computational complexity of the method. For a square, two-dimensional detector with side length of $N$ pixels, the third-order correlation function (correlations between triples of pixels) is a six-dimensional function. This must either be stored in memory or rapidly generated on-the-fly during phase retrieval, neither of which is an attractive option for working with large detectors.

We can consider a case where the sampling rate of the triple correlation may be reduced, the phase retrieved and interpolated, and combined with densely sampled diffraction data. The upscaled phase information breaks the symmetry of the real space structure autocorrelation, selecting peaks at the true atomic positions. For example, Figure 8 shows that phase information sampled at 30 pixels combined with the modulus from coherent diffraction data sampled at 200 pixels across the same region of k-space retrieves a noisy, but discernible structure.

### 6.11. Linear Phase Ramps and Sign Flips Shift and Invert the Fourier Transform

Figure 9 demonstrates the effect of linear ramps and sign flips of the phase in real space. A linear phase ramp in momentum space produces a translation in real space. A sign flip of the entire phase inverts the real space structure. Both exact numerical solving and differential evolution structure fitting obtain the phase accurately up to a linear phase ramp or sign flip (or both) in most cases, maintaining the correct relative positions but producing incorrect absolute positions and orientations.

### 6.12. Harmonic Inversion Resolves Real Space Positions from Fourier Data

In Figure 9 we used harmonic inversion to retrieve precise real space positions of the atoms from the Fourier modulus and phase. The inverse Fourier transform gives peaks with a finite width and, thus, uncertainty in the position of the atom. Harmonic inversion is not limited by the Fourier uncertainty principle and superresolves the positions of the atoms directly from the momentum space data rather than the Fourier transform [42–44].

### 6.13. 1D Phase Retrieval Example

#### 6.13.1. Exact Coherent Phase Retrieval

Using Equation 10 and the algorithm described in Section 3, we can calculate the Fourier phase from triple correlation data and compare the result to the true value. Figure 10 shows the results of phase retrieval in a simulation with a 1D pixel detector.

#### 6.13.2. Coherent Phase Retrieval via Fitting

Retrieval of the Fourier phase is highly sensitive to statistical and systematic noise. The examples of exact phase retrieval shown in the previous section were calculated for ideal experimental conditions with no sources of noise. Noise is especially problematic in the division step of Equation 10. Moreover, it is expected that the phase noise will become problematic for sources with large numbers of incoherent atoms [11]. Therefore, phase retrieval via an optimization algorithm which compares the closure phase (Equation 11) of a trial atom array to a measured closure phase may be more tractable for real experimental data.

We used a differential evolution algorithm to iterate on the spatial arrangement of the atoms until satisfactory convergence between the simulated closure phase and the closure phase of the trial structure was achieved. It can be seen in Figure 10 that the exact method based on the algorithm and the structure optimization method achieve similar results.

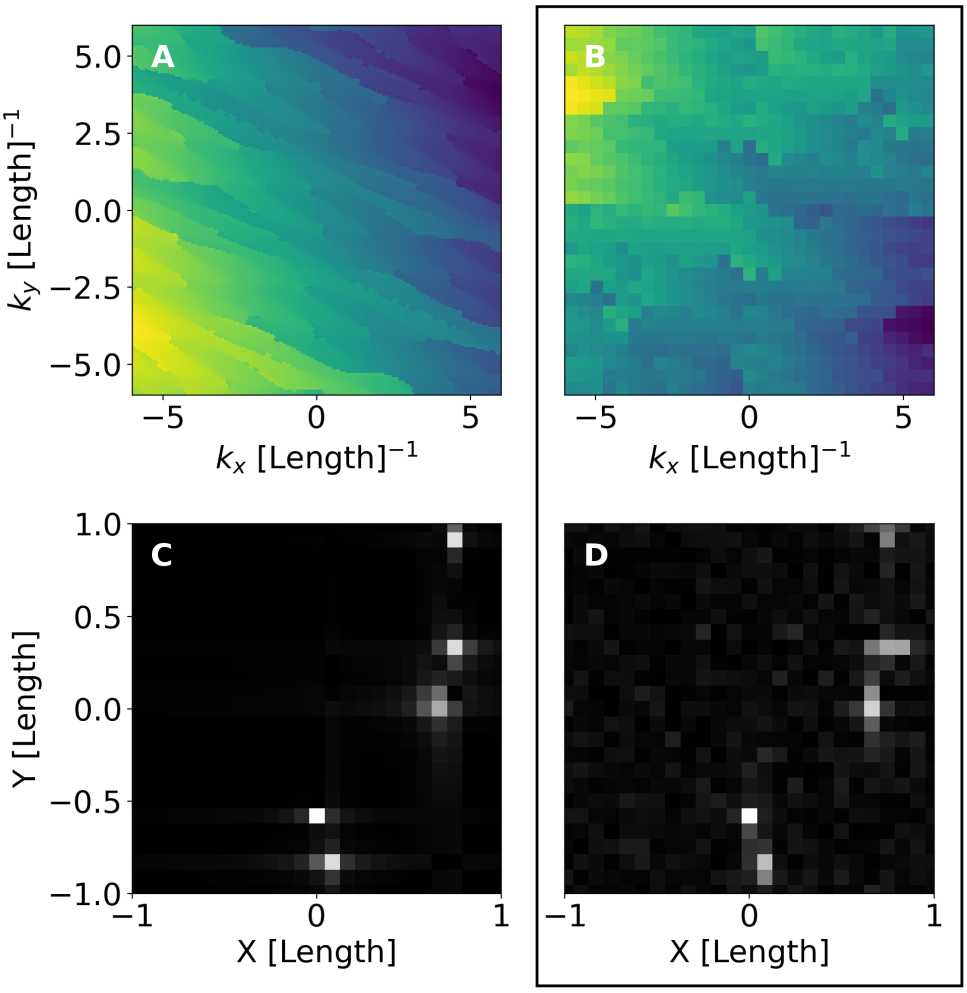


Fig. 8. (A) shows the phase $\phi(\vec{k})$ sampled and unwrapped across 201 by 201 pixels. (B) shows $\phi(\vec{k})$ sampled and unwrapped across 29 by 29 pixels on the same area of k-space. (C) is the result of taking the inverse Fourier transform using the phase shown in (A). (D) is the result of taking the inverse Fourier transform using the phase in (B) (interpolated to the same sampling resolution as in (A)) and the same modulus used to produce (C). (D) suffers from additional noise compared to (C), but each of the five atoms remains well-resolved.

### *6.14. Alternate Phase Toggling*

Figure 11 illustrates how phase toggling is implemented in the algorithm from the main text.

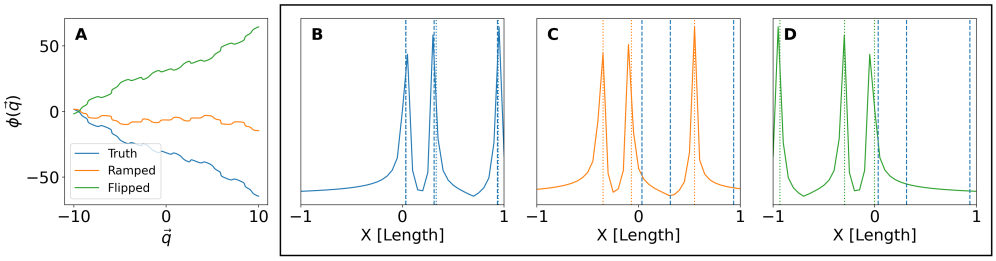


Fig. 9. (A) shows three phases which, combined with identical modulus data, produce different inverse Fourier transforms in (B), (C), and (D). The blue phase (A) and Fourier transform (B) represent the truth values. The orange phase (A) has acquired an additional linear ramp compared to the truth phase which results in a shifted Fourier transform (C) compared to the truth Fourier transform in (B). The green phase (A) has a sign flip with respect to the truth phase, causing the Fourier transform in (D) to appear inverted across the origin. Compounded ramps and sign flips of the phase result in compounded shifts and inversions of the Fourier transform. In each of (B), (C), and (D), the blue vertical dashes mark the truth positions of the atoms used in the model. The vertical dots (color matches color of phase pictured in (A)) indicate the atom positions calculated via harmonic inversion of the modulus and phase. In the case of (B), harmonic inversion determines the truth positions of the atoms quite accurately. In (C) and (D), sub-linewidth positions of the shifted and inverted atom array are shown to maintain the correct interatomic separations. The Fourier transforms (solid curves) are each normalized to the height of the tallest peak.

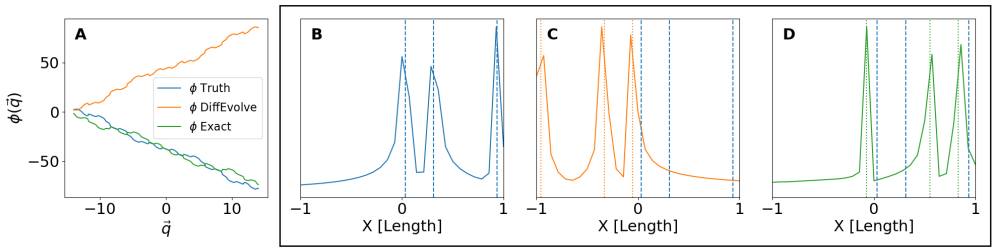


Fig. 10. Phase retrieval results compared to truth values (blue) for a 1D array of three atoms using the exact numerical solution (green) of Section 3 and differential evolution (orange). (A) shows the retrieved (orange and green) and truth (blue) phases used, together with the modulus obtained from Equation 8, to execute the inverse Fourier transform in (B), (C), and (D). In (B), the truth object from the inverse Fourier transform and the known positions (vertical dots) of the atoms match, unsurprisingly. (C) shows that differential evolution correctly found atom positions (orange vertical dots) with the correct separation and ordering, but the structure appears flipped and shifted compared to the truth positions (blue vertical dots). This is due to the linear phase ramp in (A) compared to the truth phase. The effect of linear phase ramps and sign flips is detailed in Appendix 6.11. Similarly, the exact numerical solution in (D) also retrieved the correct interatomic separations but the phase (green) in (A) is inverted to the truth phase, causing a flip of the real space structure. Since the exact numerical algorithm finds the phase without directly determining atom positions, we used harmonic inversion (see Appendix 6.12) to determine a sub-linewidth position for the three atoms (green vertical dots) to compare to the truth atom positions (blue vertical dots). The Fourier transforms (solid curves) are each normalized to the height of the tallest peak.

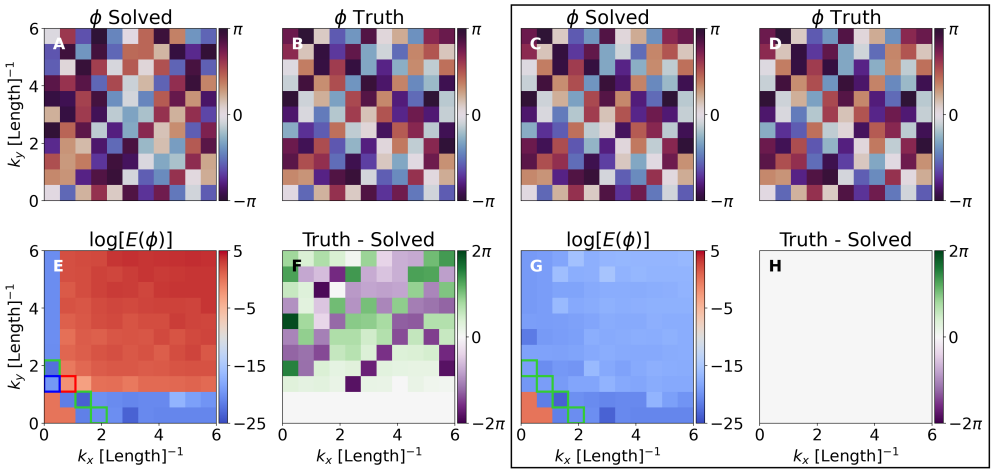


Fig. 11. In these examples, the value of $\phi(\vec{k})$ in (A) and (C) in each diagonal $k_y = -k_x + n, n \in \mathbb{Z}$ is determined beginning at the origin and ending in the upper right corner. In the first example (left), where toggling is not used, the solved value of $\phi$ in (A) has a large difference (F) from the true value of $\phi$ in (B). We observe that the value of $\log[E(\phi)]$ (E) is seen to spike (red box) along the third diagonal (green and red boxes). The value of the error function increases and propagates to surrounding pixels as additional diagonals are solved. This indicates that a pixel in the second diagonal (blue box) has been assigned incorrectly. Resolving the second diagonal by substituting alternate minima of $\log[E(\phi)]$ eventually arrives at a $\phi(\vec{k})$ (C) which has uniformly low values of the error function (G) such that the difference (H) between the solution (C) and truth (D) is quite small. Note that the error function, (E) and (G), is defined to be zero at the origin and the origin nearest neighbors as these values of $\phi(\vec{k})$ are free parameters of the solution process.